Electroproduction of the d^* dibaryon

Chun Wa Wong
Department of Physics and Astronomy, University of California, Los Angeles, California 90095-1547
(Received 31 January 2000; published 19 May 2000)

The unpolarized cross section for the electroproduction of the isoscalar $J^\pi=3^+$ didelta dibaryon d^* is calculated for a deuteron target using a simple picture of elastic electron-baryon scattering from the $\Delta\Delta(^7D_1)$ and the $NN(^3S_1)$ components of the deuteron. The calculated differential cross section at the electron laboratory energy of 1 GeV has a value of about 0.24 (0.05) nb/sr at the laboratory angle of 10° (30°) for the Bonn B potential when the dibaryon mass is taken to be 2.1 GeV. The cross section decreases rapidly with increasing dibaryon mass. A large calculated width of 40 MeV for $d^*(\Delta\Delta\ ^7S_3)$ combined with a small experimental upper bound of 0.08 MeV for the d^* decay width appears to have excluded any low-mass d^* model containing a significant admixture of the $\Delta\Delta(^7S_3)$ configuration.

PACS number(s): 14.20.Pt, 25.30.Dh, 13.85.Fb

I. INTRODUCTION

Given the availability of excellent electron beams, the electroproduction of dibaryon resonances [1] represents a promising way to look for these long-sought-for objects [2,3]. In assessing the practical prospects of such experiments, one needs to begin with rough estimates of the electroproduction cross sections. This has to be done separately for each dibaryon candidate of interest, since each candidate may involve unique theoretical issues.

One candidate dibaryon that has been discussed recently is the didelta d^* of quantum numbers $J^\pi T=3^+0$ [4–7]. This dibaryon is a six-quark state which at large interbaryon separations may be visualized as a pair of Δ's. Preliminary studies of its electroproduction from deuteron targets have recently been made by Qing [8] and by Sun [9], both of Nanjing University. They find that the Kroll-Ruderman $\gamma d \rightarrow \Delta\Delta$ production process does not contribute because of the special isospin structure of d and d^*. They concentrate instead on another process important in the electroproduction of two pions from a proton [10] and a deuteron [11] based on the electroexcitation of a nucleon isobar $N^*(1520)$ in the intermediate state, namely, $\gamma d \rightarrow NN^*(1520) \rightarrow \Delta\Delta$. This mechanism can be interpreted as the production of d^* through its NN^* component.

However, these preliminary results for the calculated differential cross sections turn out to be very small at small momentum transfers (say, <500 MeV/c), almost two orders of magnitude smaller than a simple estimate made by me using a simple picture of inelastic scattering from the $\Delta\Delta(^7D_1)$ of the deuteron, as described in diagram (a) of Fig. 1. These results seem to suggest that d^* is more easily produced from the deuteron at these small momentum transfers through elastic electron-baryon (eB) scatterings rather than inelastic excitations of the struck baryon.

It is worth noting in connection with diagram 1(a) that if the d^* is visualized as a $^7S_3$ didelta, there is no production from the deuteron $\Delta\Delta(^3S_1)$ component in the lowest order. This is because the electromagnetic operators are of rank only 0 or 1 in intrinsic spin. Hence electroproduction in this simple lowest-order picture is possible only from the $\Delta\Delta(^7D_1)$ component of the deuteron.

In addition to diagram 1(a), or equivalently its perturbative part diagram 1(b), d^* can also be electroproduced through the $NN(^3D_3-^3G_3)$ component of d^*, as described in diagram 1(c). Lomon has looked for a d^* resonance in these channels by studying the energy dependence of their NN phase parameters [12,13]. These $NN(^3D_3-^3G_3)$ channels are in fact the dominant decay channels of d^* [7,14,15]. He has found that these phase parameters are consistent with the absence of any dibaryon resonance with a width exceeding 1 (2) MeV near 2.1 (2.25) GeV.

A much stricter upper limit on the width of an np dibaryon resonance was obtained experimentally some time ago by Lisowski *et al.* [16]. They measured the total np cross section at c.m. energies 2.00–2.23 GeV at high-energy resolution, namely, about 1.4 MeV at 2.11 GeV. No evidence was seen for narrow resonances with areas greater than 5 mb MeV. At 2.1 GeV where the np $I=0$ total cross section is 33 mb, a totally elastic $^3D_3$ resonance would have a maximum unitarity-limited cross section of $\sigma_{\max}=39$ mb. Its energy-integrated area is $(\pi/2)\sigma_{\max}\Gamma$ for a pure Breit-Wigner shape, where Γ is its total decay width. The assumption of a pure Breit-Wigner resonance should be a very good one, because the NN $^3D_3$ phase shift at the total energy of 2.1 GeV is only 4° [12]. The experimental bound of 5 mb MeV on the integrated area translates to an upper bound of only 0.08 MeV for the width of any resonance that has escaped detection in this experiment.

The theoretical decay width of d^* has been estimated in [7]. If the d^* is taken to be a bound system of two finite-sized Δ's, describable by a nonrelativistic quark model, the decay has been estimated to be about 10 MeV when its mass is 2.1 GeV. The result is, however, sensitive to both dynamical input and rescattering corrections; it could be as large as 40 MeV for a realistic potential treated perturbatively without any rescattering correction, as I shall show in more detail in this paper.

It has been argued in [7] that if the dibaryon is made up of six delocalized quarks [4–6] instead of two separated Δ's, its decay width could well be smaller by an order of magnitude, say, 1 MeV. This suggestion remains to be confirmed by a detailed calculation. A reduction to 0.1 MeV would be much harder to realize. Furthermore, if the estimated decay width

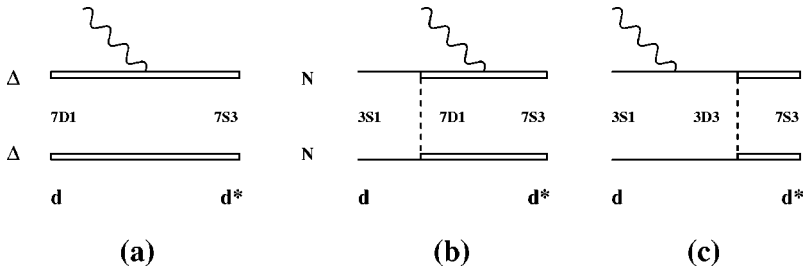

FIG. 1. Electroproduction of d^* from the deuteron (a) from the deuteron $\Delta\Delta\,{}^7D_1$ state, (b) from the perturbative deuteron $\Delta\Delta\,{}^7D_1$ wave function, and (c) from the deuteron ${}^3S_1$ state to the perturbative $d^*(NN\,{}^3D_3)$ wave function.

has to be reduced for any reason, its estimated production cross sections, including the electroproduction cross section estimated here using a didelta model, must also be reduced correspondingly.

Thus the case for a d^* resonance near 2.1 GeV does not appear promising. However, the d^* could have a mass higher than expected if the dynamics is different from that described by the delocalization and color-screening model. Hence it is still of interest to study the electroproduction cross section for d^*, should such a resonance exist.

It is obvious that in addition to diagram 1(a) or 1(b), one should also include the process shown in diagram 1(c), where the d^* is produced through the $NN({}^3D_3)$ channel, the $NN({}^3G_3)$ contribution having been ignored in this lowest-order picture.

Although these two processes alone do not add up to a quantitative description of the electroproduction, they are of sufficient interest to justify the detailed report given here, including the contributions of convective and magnetization currents. The picture is necessarily very rough, because of the neglect of many components and processes. However, uncertainties about the mass and structure of d^* and about short-distance nuclear dynamics have discouraged me from undertaking a more ambitious calculation at this time.

The paper is organized as follows: The notation used is defined in Sec. II where brief comments relevant to the present calculation are made. Section III shows how the calculation is done for diagram 1(a), when the needed $\Delta\Delta({}^7D_1)$ component of the deuteron is already available. The contributions from different reduced matrix elements (RME's) are briefly discussed.

Section IV shows that the inclusion of the $d^*(NN\,{}^3D_3)$ contribution via the perturbative process, Fig. 1(c), can be broken down into three steps: (a) a perturbative evaluation of the $d^*(NN\,{}^3D_3)$ wave function, (b) a calculation of the d^* decay width for the same input dynamics (taken to be the 28-channel Argonne potential [17] and the Bonn B potential [18]), and finally (c) evaluation of the electroproduction cross section itself.

Calculational results are presented in Sec. V, where the production amplitude from diagram 1(c) is found to be greater than that from diagram 1(a) by a factor of 2–4 at certain angles or momentum transfers. At a laboratory angle of 30° and an electron laboratory energy of 1 GeV, I find a differential production cross section of about 0.05 nb/sr when integrated over the energy loss.

My calculated cross section is smaller by two orders of magnitude from the preliminary value of about 10 nb/sr obtained recently by Qing, Sun, and Wang (to be called QSW) [19] using a different method of calculation. Part of the discrepancy, accounting for a factor of 5, comes from the fact that QSW has included only π exchange but not ρ exchange. The remaining discrepancy, of more than an order of magnitude, must be due to differences in calculational methods used. For example, I use a principal-value Green function for two nucleons in the $d^*(NN\,{}^3D_3)$ wave function, whereas QSW use an outgoing-wave boundary condition. To help in disentangling the discrepancy in the future, I have included many details in the present paper.

The decay width calculated here for the $\Delta\Delta({}^7S_3)$ model of d^* is about 40 MeV at $m^*=2.1$ GeV. When used with the experimental upper bound of only 0.08 MeV of any $I=0$, $J=3$ np resonance [16], the calculated width makes it very unlikely that any undetected d^* has a significant probablity of the $\Delta\Delta({}^7S_3)$ configuration.

II. ELECTROPRODUCTION CROSS SECTION FOR $ed\rightarrow ed^*$

Consider the scattering of a relativistic electron beam of laboratory energy ϵ to the laboratory angle θ by a target that goes from an initial state i to a final state f as the result of the scattering. The differential cross section in the laboratory (after integrating over the energy transfer) is known to have the form [20]

$$\frac{d\sigma_{fi}}{d\Omega}=\sigma_M f_{\rm rec}^{-1}[v_L T_{fi}^L+v_T(T_{fi}^{\rm el}+T_{fi}^{\rm mag})], \tag{1}$$

where

$$\sigma_M=\left[\frac{\alpha\cos(\theta/2)}{2\epsilon\sin^2(\theta/2)}\right]^2 \tag{2}$$

is the Mott differential cross section, α is the fine structure constant,

$$f_{\rm rec}=1+\frac{2\epsilon\sin^2(\theta/2)}{M_{\rm target}} \tag{3}$$

is a target recoil factor, and

$$v_L=\left(\frac{Q^2}{q^2}\right)^2,\quad v_T=-\frac{1}{2}\left(\frac{Q^2}{q^2}\right)+\tan^2\left(\frac{\theta}{2}\right) \tag{4}$$

are the electron kinematical factors that depend on its four-momentum transfer $Q=K-K'=(\omega,\mathbf{q})$. Here $K=(\epsilon,\mathbf{k})$ is the four-momentum of the electron in the laboratory before

the scattering, and K' its four-momentum after the scattering. The notation is that of [21], with $Q^2 \leqslant 0$.

The target factors are

$$T_{fi}^{L} = \frac{4\pi}{2J_i+1} \sum_{J=0}^{\infty} |\langle J_f \| \hat{M}_J(q) \| J_i \rangle|^2,$$

$$T_{fi}^{\alpha} = \frac{4\pi}{2J_i+1} \sum_{J=1}^{\infty} |\langle J_f \| \hat{T}_J^{\alpha}(q) \| J_i \rangle|^2, \tag{5}$$

where $\alpha =$ ''el'' or ''mag.'' The nuclear RME's $\langle J_f \| \mathcal{O} \| J_i \rangle$ that appear are all dimensionless quantities. The operators $\mathcal{O}$ are the longitudinal Coulomb, and the transverse electric and magnetic, multipole operators that have the following simple forms in momentum space [8]:

$$\hat{M}_J(q) = \frac{(-i)^J}{4\pi} \int d\Omega_{\mathbf{q}} Y_J(\Omega_{\mathbf{q}}) \rho(\mathbf{q}),$$

$$\hat{T}_J^{\mathrm{el}}(q) = -\sqrt{8\pi} \sum_{\kappa} \langle \kappa \| Y_J \| 1 \rangle \begin{Bmatrix} 1 & 1 & 1 \\ J & J & \kappa \end{Bmatrix} \times \frac{(-i)^J}{4\pi} \int d\Omega_{\mathbf{q}} [Y_{\kappa}(\Omega_{\mathbf{q}}) \otimes \hat{\mathbf{J}}(\mathbf{q})]^J,$$

$$\hat{T}_J^{\mathrm{mag}}(q) = \frac{(-i)^J}{4\pi} \int d\Omega_{\mathbf{q}} [Y_J(\Omega_{\mathbf{q}}) \otimes \hat{\mathbf{J}}(\mathbf{q})]^J. \tag{6}$$

Here Y_J is a spherical harmonic, and $\rho(\mathbf{q})$ and $\hat{\mathbf{J}}(\mathbf{q})$ are the baryon charge and current density operators.

The current density operator can be separated into convective and magnetization terms:

$$\hat{\mathbf{J}}(\mathbf{q}) = \hat{\mathbf{J}}_{\mathrm{c}}(\mathbf{q}) + \hat{\mathbf{J}}_{\mathrm{S}}(\mathbf{q}). \tag{7}$$

The spin magnetization term $\hat{\mathbf{J}}_S = \boldsymbol{\nabla} \times \hat{\boldsymbol{\mu}}_S$ originates from the dibaryon isoscalar magnetic moment operator $\hat{\boldsymbol{\mu}}_S = \mu_0 \mu_s \hat{\mathbf{S}}$. Here μ_0 is the nuclear magneton, and $\hat{\mathbf{S}}$ is the total spin angular momentum operator of the nucleus. In this notation, the nucleon magnetic-moment operator is written as $\hat{\boldsymbol{\mu}}(N) = \mu_0 [\mu_s(N) \hat{\mathbf{S}} + \mu_v(N) \hat{\boldsymbol{\tau}}_3 \hat{\mathbf{S}}]$, while the isoscalar part of the operator for Δ is $\mu_0 \mu_s(\Delta) \hat{\mathbf{S}}$. The isoscalar baryon magnetic-moment parameters used are the experimental value

$$\mu_s(N) = \mu_p + \mu_n = 0.880, \tag{8}$$

for the nucleon, and the theoretical value from the nonrelativistic quark model

$$\mu_s(\Delta) = \mu_v(N)/5 = 0.94, \tag{9}$$

for the Δ. This quark model actually gives the same value for both baryon isoscalar magnetic moments. I prefer to use the slightly larger value shown for $\mu_s(\Delta)$ obtained from the experimental nucleon isovector magnetic moment of $\mu_v(N) = \mu_p - \mu_n = 4.71$.

As is known [22], the orbital magnetization term is already contained in $\hat{\mathbf{J}}_c$, and does not have to appear explicitly.

For specific components in the initital and final nuclear states, only a few terms are allowed in the multipole sum shown in Eq. (5) by the triangle rule for angular momenta. For the dibaryon components included in our calculations, the relative BB orbital angular momenta of initial and final nuclear states (L_i, L_f) are either (0,2) or (2,0). Then only the $J=2$ multipole term appears for the Coulomb target factor.

The situation for the transverse RME's is slightly more complicated. It is controlled by the spatial RME

$$\left\langle L'=0 \left\| \int d\Omega_{\mathbf{q}} [Y_{\kappa}(\Omega_{\mathbf{q}}) \otimes \overline{\mathbf{p}}]^{\lambda} \right\| L=2 \right\rangle = \delta_{\lambda 2} \sum_{\kappa=1,3} f_{\kappa}(q), \tag{10}$$

where $\overline{\mathbf{p}} \equiv \mathbf{p} + (\mathbf{q}/4)$ is the mean of the initial relative BB momentum $\mathbf{p}$ and its final value $\mathbf{p} + (\mathbf{q}/2)$ after the absorption of a virtual photon of momentum $\mathbf{q}$. Part of the photon momentum, $\mathbf{q}/2$, goes into the recoil of the dibaryon. The functions $f_{\kappa}(q)$ are not needed at this point, and will not be given. The important features are that the operator must be a spatial quadrupole operator, and that κ can only be 1 or 3.

Equation (10) has the consequence that the only operators contributing to the transverse RME for the dibaryon wave functions used in the present study are (a) the convective and orbital magnetization current terms in $\hat{T}_{J=2}^{\mathrm{el}}$, (b) the spin magnetization current term in $\hat{T}_J^{\mathrm{el}}$, with $J=2$ and 3, and (c) the spin magnetization current term in $\hat{T}_{J=3}^{\mathrm{mag}}$.

III. CONTRIBUTIONS OF THE DEUTERON $\Delta\Delta(^7D_1)$ COMPONENT

The d^* dibaryon will be treated in this paper as a pure $\Delta\Delta(^7S_3)$ state, using the two-centered Gaussian wave function parametrized in [15] as a sum of Gaussians. This wave function will be specified with other wave functions used in this paper in the Appendix.

The inelastic production of d^* from the deuteron $\Delta\Delta(^7D_1)$ component in the initial state by elastic $e\Delta$ scattering is described by diagram 1(a). The Argonne-28 (A28) deuteron $\Delta\Delta(^7D_1)$ wave functions [23] are used, expanded in harmonic-oscillator wave functions (HOWF's).

However, it is sufficient to give explicit expressions for the RME's appearing in the differential production cross section only for single-term wave functions such as the single Gaussian

$$\psi_{d^*}(\mathbf{p}) = N_0^* e^{-p^2/2\beta^{*2}} \tag{11}$$

for d^*. Here

$$N_0^* = (\pi \beta^{*2})^{-3/4}. \tag{12}$$

For the deuteron $\Delta\Delta(^7D_1)$ component, a one-term form of the HOWF's is

$$\psi_d(\mathbf{p}, \Delta\Delta, ^7D_1) = \sqrt{P_{\Delta\Delta 7}} N_2 e^{-p^2/2\beta^2} \mathcal{Y}_{2m}(\mathbf{p}), \tag{13}$$

where $P_{\Delta\Delta 7}$ is the $\Delta\Delta(^7D_1)$-state probability of the deuteron,

$$N_2=\left(\frac{16\pi}{15\beta^4}\right)^{1/2}(\pi\beta^2)^{-3/4}, \tag{14}$$

and $\mathcal{Y}_{2m}(\mathbf{p})=p^2Y_{2m}(\hat{\mathbf{p}})$ is a solid spherical harmonic. Then the Coulomb RME is

$$\langle d^*\|\hat{M}_2(q)\|d_7\rangle=\sqrt{3/5}\langle d^*,S\|\hat{M}_2(q)\|d_7,D\rangle$$
$$=-\frac{\sqrt{3}}{4\pi}(\lambda q)^2 f(q), \tag{15}$$

where d_7 stands for the deuteron $\Delta\Delta(^7D_1)$ component:

$$\lambda=\frac{a^*}{2(a^*+b)}, \tag{16}$$

$$f(q)=\sqrt{P_{\Delta\Delta}}N_0^*N_2\left(\frac{\pi}{a^*+b}\right)^{3/2}\mathrm{e}^{-cq^2/2}, \tag{17}$$

$$a^*=(2\beta^{*2})^{-1},\quad b=(2\beta^2)^{-1},$$

$$c=\lambda b+\alpha_0,\quad \alpha_0=r_p^2/3=0.12\ \ \mathrm{fm}^2. \tag{18}$$

The α_0 term takes care of the baryon form factor at the γ-baryon vertex. If the Δ is assumed for simplicity to have the same size as the nucleon, the same Gaussian form factor appears in all terms of the production amplitude in the nonrelativistic quark model. Additional baryon form factors that should appear are already included in the BB interactions themselves.

The transverse RME's can be separated into convective and spin magnetization terms:

$$\langle d^*\|\hat{T}^{\mathrm{el}}_{c2}(q)\|d_7\rangle=-\frac{\sqrt{2}}{4\pi}\frac{1}{M_B}g_\lambda(q)f(q),$$

$$\langle d^*\|\hat{T}^{\mathrm{el}}_{\mu 2}(q)\|d_7\rangle=-[\mu_s(B)\mu_0/\pi]f(q)[g_\lambda(q)-g_\nu(q)], \tag{19}$$

where $B=\Delta$ in M_B and $\mu_s(B)$, and

$$g_\lambda(q)=\frac{3\lambda q}{2(a^*+b)},\quad g_\nu(q)=\lambda^2\nu q^3,\quad \nu=\frac{1}{4}-\lambda, \tag{20}$$

$$\langle d^*\|\hat{T}^{\mathrm{mag}}_{c3}(q)\|d_7\rangle=0,$$

$$\langle d^*\|\hat{T}^{\mathrm{mag}}_{S3}(q)\|d_7\rangle=-\sqrt{8/7}\frac{\mu_0}{4\pi}\mu_s(B)g_\nu(q)f(q). \tag{21}$$

I use a three-term approximation to the deuteron $\Delta\Delta(^7D_1)$ wave function of the Argonne 28-channel potential [17,23], denoted below as potential A28. The approximate wave function used is given in the Appendix.

It is convenient to present the calculated results not as angular distributions which contain strong dependence on the electron energy, but as the effective T factor

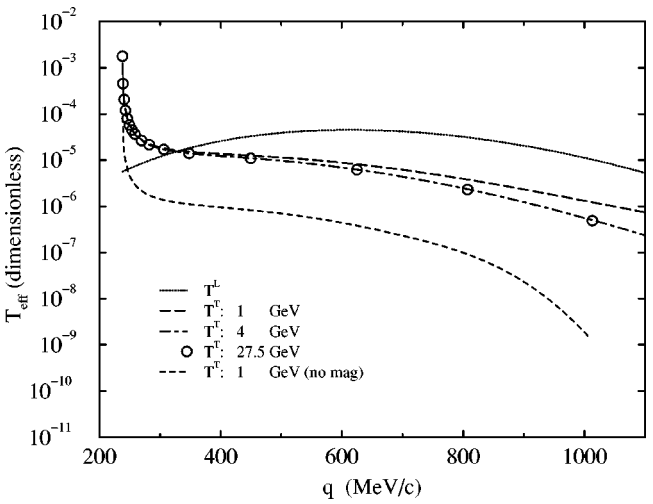

FIG. 2. The effective T factors appearing in the differential electroproduction cross section of d^* from the deuteron at different electron laboratory energies as calculated from diagram 1(a) for potential A28.

$$T_{\mathrm{eff}}=T^L_{fi}+(v_T/v_L)(T^{\mathrm{el}}_{fi}+T^{\mathrm{mag}}_{fi}). \tag{22}$$

The Coulomb T factor T^L is a function only of the three-momentum transfer q, and is energy independent in our model. The transverse terms contain the kinematical factor v_T/v_L, but the energy dependence from the angle-dependent term is small except at low electron energies.

The weak energy dependence of these effective T factors is explicitly illustrated in Fig. 2 for a d^* mass m^* of 2100 MeV and for three different electron energies. The A28 $d(\Delta\Delta\,^7D_1)$ wave function is used. The three-momentum transfer has the energy-independent minimal value of $q_{\min}\approx 238$ MeV/c at this value of m^*. The momentum range shown corresponds to an angular range of about 90° (15°, 2°) for 1 GeV (4 GeV, 27.5 GeV) electrons.

In the transverse electric T factor, the amplitude from the magnetization current is a factor of 2.5 or 3 larger than that from the convective current. This means that the electric T factor is larger by roughly an order of magnitude when the contribution from the magnetization current is included.

On the other hand, the transverse magnetic T factor is very small at small angles, but has become 1/3 as large as the transverse electric T factor at $q\approx 1$ GeV/c.

The calculated cross section for diagram 1(a) is proportional to the probability $P_{\Delta\Delta 7}$ of the $\Delta\Delta(^7D_1)$ component of the deuteron, other things being equal. Besides the A28 model, the Argonne group has constructed a weaker model with $P_{\Delta\Delta 7}=0.23\%$ instead of 0.42%. The coupled-channel models E and F constructed by Dymarz and Khanna [24] have $P_{\Delta\Delta 7}\approx 0.1$–$0.4\,\%$, and a total $P_{\Delta\Delta}\approx 0.4$–$0.5\,\%$. The relativistic field-theory model studied by Ivanov *et al.* [25] gives a total $P_{\Delta\Delta}$ of only 0.08%.

These theoretical estimates are consistent with the best experimental information on the total $P_{\Delta\Delta}$, namely, that it does not exceed 0.4% at 90% C.L. from the null result of a bubble chamber search for the spectator Δ^{++} in a νd knockout reaction [26].

IV. INCLUSION OF THE $NN(^3D_3)$ COMPONENT OF d^*

Although diagram 1(c) has a structure rather similar to that for diagram 1(b), its production amplitudes are much harder to calculate because of three complications: (1) The wave function in the minor component $d^*(NN\,^3D_3)$ needed in the calculation is not to our best knowledge readily available in the literature. It has to be evaluated *ab initio*. (2) This wave function is very sensitive to the spreading width Γ of $d^*(\Delta\Delta\,^3S_3)$ into NN channels. Although the production cross section turns out to be only mildly dependent on Γ, it is desirable to use the width consistent with the assumed input dynamics in the calculation. This too has to be evaluated. (3) The wave function has sharp kinks near p_0 where the nucleon energy $E_N(p_0)$ has the value $m^*/2$. We find it simpler to perform a one-dimensional integration for the production amplitudes instead of using the harmonic-oscillator expansion described in the last section.

The calculation is thus broken up into three major steps in order to handle the three complications listed above.

A. Perturbative treatment of wave-function components

Our first concern is to estimate the accuracy of a perturbative treatment of $d^*(NN\,^3D_3)$. This is done by first examining a similar perturbative generation of the $d(\Delta\Delta\,^7D_1)$ from $d(NN\,^3S_1)$ using the Argonne-28 potential from [17]

$$\begin{aligned}\psi(\Delta\Delta\,^7D_1,p)&\equiv\langle\Delta\Delta\,^7D_1,p|d\rangle\\&\approx\left\langle\Delta\Delta\,^7D_1,p\left|\frac{1}{\Delta H}V\right|d(NN\,^3S_1)\right\rangle\\&=\frac{1}{m_d-2E_\Delta(p)}\frac{1}{(2\pi)^3}\\&\quad\times\int\langle\Delta\Delta^7D_1|\mathcal{O}_{18}(\hat{\mathbf{q}})|NN\,^3S_1\rangle\\&\quad\times v_{18}(q)\langle\mathbf{p}+\mathbf{q}|d(NN\,^3S_1)\rangle d^3\mathbf{q}.\end{aligned}\tag{23}$$

Here $\Delta H=m_d-H_0$, with H_0 the unperturbed Hamiltonian and m_d the deuteron mass, $E_\Delta(p)$ is the nonrelativistic Δ energy, and $\mathcal{O}_{18}(\hat{\mathbf{q}})$ is the $NN\leftrightarrow\Delta\Delta$ tensor-force operator $S_{12}^{\rm III}(\hat{\mathbf{q}})\mathbf{T}_1\cdot\mathbf{T}_2$ in the A28 notation with $\mathbf{T}_i$ the $N\leftrightarrow\Delta$ isospin operator. The subscript 18 refers to channel 18 of A28. The momentum-space potential is

$$v_{18}(q)=-v_{\pi0}^{\rm III}\frac{4\pi}{\mu^3}\frac{q^2}{q^2+\mu^2}f(q),\tag{24}$$

where $\mu=138$ MeV is the pion mass, $v_{\pi0}^{\rm III}=14.91$ MeV, and $f(q)$ is a numerically generated cutoff function that decreases from 1 at $q=0$ to 0 at $q=\infty$.

Equation (23) can be simplified to a one-dimensional integral if the deuteron $NN(^3S_1)$ wave function is expanded as a sum of Gaussians. It is sufficient to give the final expression for a single Gaussian wave function of the form of Eq. (11), but with falloff parameter β and an associated normalization constant N_0 if the S-state probability were 100%. Then

$$\psi_7(p)\equiv\psi(\Delta\Delta\,^7D_1,p)\approx\frac{h(p)}{m_d-2E_\Delta(p)},\tag{25}$$

where the subscript 7 refers to the spin degeneracy,

$$h(p)=\sqrt{\frac{28}{5\pi^3}}N_0e^{-p^2/2\beta^2}\int v_{18}(q)e^{-q^2/2\beta^2}j_2(ix)q^2dq,\tag{26}$$

and $x=pq/\beta^2$.

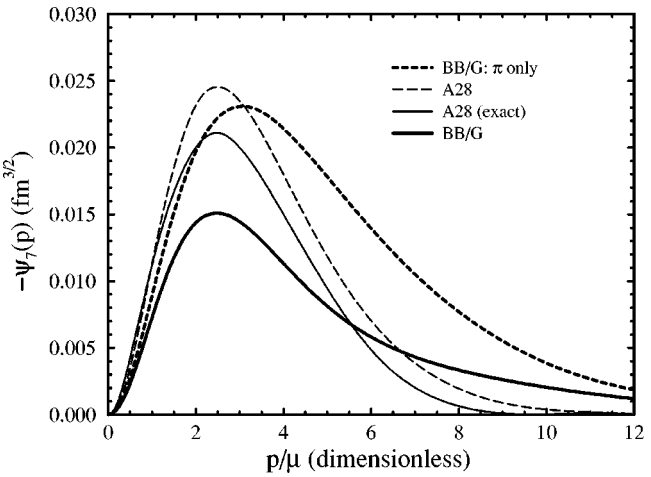

FIG. 3. Comparison of the perturbative wave functions $\psi_7(p)$ in momentum space of the deuteron $\Delta\Delta\,^7D_1$ state for the potentials A28 and BB/G to the exact value for the A28 potential. Here $\mu=138.0$ MeV is the pion mass.

The actual calculation is made with a three-term fit to the A28 deuteron $NN(^3S_1)$ wave function [17,23] given in the Appendix. The resulting deuteron $\Delta\Delta(^7D_1)$ wave function calculated from Eq. (25) (long dashed curve) is compared in Fig. 3 with the actual A28 wave function (solid curve) in the fitted form given by Eqs. (A1)–(A3). The wave function is so defined that $\int\psi_7^2(p)p^2dp$ gives the fractional normalization P_7 in this $\Delta\Delta(^7D_1)$ state. The calculated value in the perturbative approximation is $P_7=0.65\%$ compared to the exact value of 0.419%.

One can see from Fig. 3 that the inaccuracy in the perturbative treatment comes from the overestimate of the wave function at all momenta larger than $\approx1.3\mu$, where $\mu=138.0$ MeV is the average pion mass used in these calculations. The error seems to arise primarily from the neglect of a short-range repulsive central potential in the $\Delta\Delta(^7D_1)$ channel. Such a repulsive potential would have reduced the wave function at small interbaryon distances. The size of the error in our perturbative treatment in this $^7D_1$ state seems to be much greater than the results found by [24]. We shall see that there are much greater uncertainties elsewhere in the present calculation. Consequently, I shall consider the accuracy of the perturbative treatment adequate for the present qualitative study.

The same perturbative method is now used to obtain the $NN(^3D_3)$ component of d^*. An added complication appears because the $\Delta\Delta(^7S_3)$ component of d^* is a bound state embedded in the NN continuum. The calculation will require the use of a spreading width into the NN continuum (which is essentially just the total width Γ of d^*) and a principal-value Green's function. The matrix element of the tensor-force operator is also different from Eq. (23). The final result is rather similar to Eq. (25):

$$\psi_3(p) \equiv \langle NN^3D_3, p | d^* \rangle \approx \frac{\Delta E}{(\Delta E)^2 + (\Gamma/2)^2} h^*(p), \tag{27}$$

where $\Delta E(p) = m^* - 2E_N(p)$,

$$h^*(p) = \sqrt{\frac{12}{5\pi^3}} N_0^* e^{-p^2/2\beta^{*2}} \times \int v_{18}(q) e^{-q^2/2\beta^{*2}} j_2(ix^*) q^2 dq, \tag{28}$$

and $x^* = pq/\beta^{*2}$.

In Eq. (27), a rapidly changing factor $\Delta E/[(\Delta E)^2 + (\Gamma/2)^2]$ has been separated from a function $h^*(p)$ that does not depend explicitly on m^* or Γ. Here ΔE changes sign as the nucleon momentum p increases above that value p_0 at which $\Delta E(p)$ vanishes. Above p_0, ΔE is negative so that the perturbative wave function $\psi_3(p)$ tends to have the same phase relation to the driving $\Delta\Delta(^7S_3)$ wave function as $\psi_7(p)$ is to its own driving wave function. This means that diagrams 1(b) and 1(c) tend to interfere constructively at large momentum transfers, but destructively at small momentum transfers.

The falloff parameter β^* and normalization constant N_0^* appearing in Eq. (28) are those for the single-Gaussian approximation to the $d^*(\Delta\Delta\,^7S_3)$ wave function.

In the actual calculation, a three-term Gaussian fit to the two-centered d^* wave function is used. The results for potential A28 are shown as long dashed curves in Fig. 4 for $h^*(p)$ and the radial part $\psi_3(p)$ of Eq. (27) calculated with $m^* = 2100$ MeV and $\Gamma = 100$ MeV. This spin-triplet wave-function component has the perturbative normalization of $P_3 = 0.038$, or 3.8%. This normalization is very sensitive to the choice of the decay width, increasing to 0.55 if the width is decreased to 10 MeV. The rapid increase comes from the roughly $1/\Gamma$ behavior of the amplitude of the kink where the wave function oscillates rapidly from a positive value to a negative value as the momentum p goes through the zero of ΔE.

The great sensitivity of the $^3D_3$ wave function to the width Γ does not mean that the inelastic production amplitude increases just as dramatically. The wave function changes sign in the kink, leading to much cancellation in its contribution to the inelastic RME. Consequently, most RME's increase by only 25% when the width decreases from 100 MeV to 10 MeV, and approach stable values for smaller widths.

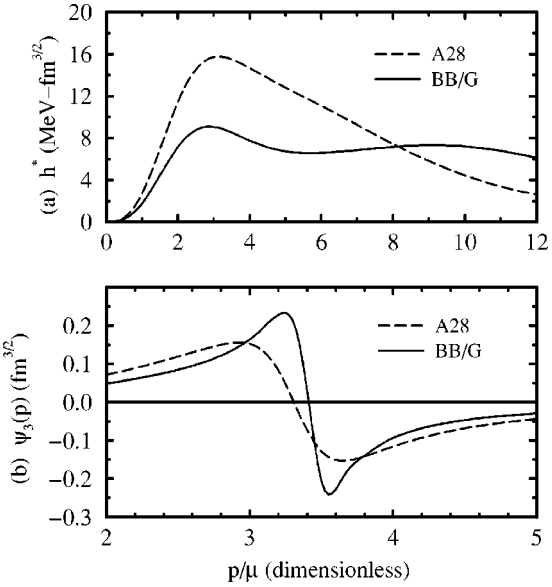

FIG. 4. The perturbative wave functions of the $d^*(NN\,^3D_3)$ state for the potentials A28 and BB/G showing (a) the smooth function $h^*(p)$ and (b) the wave function $\psi_3(p)$ in momentum space. Here $\mu = 138.0$ MeV is the pion mass.

Although the dependence on Γ as described above is technically correct in a narrow sense, it is also counterintuitive in that a smaller width with weaker coupling to the NN channel somehow leads to a stronger $^3D_3$ component. The truth is that in the discussion just given, the width is treated as if it were a free parameter when it actually is not. Rather, once the dynamics is chosen, a certain width is implied, and must be used in Eq. (27).

Hence it is desirable to have a more consistent treatment. I shall first calculate the width for each input potential at each dibaryon mass m^*, and then use this calculated width to calculate admixed components.

B. Decay width of d^*

The decay width of d^* into the NN (πNN, $d\pi\pi$) channel has been estimated in [7] ([14], [15]). It is clear that the NN channel is by far its dominant decay channel; it is the only channel that has to be included in the present study. The d^* decay widths into NN for the A28 potential [17] and five different Bonn potentials [27,18] are easily calculated by the same method. The results are shown in Table I for $m^* = 2100$ MeV and a single-Gaussian wave function for d^* of radius $r^* = 0.7$ fm.

The potentials are ordered in Table I in decreasing values of their deuteron D-state probability P_D. The differences in P_D have been obtained by adjusting the amount of short-range repulsion in the tensor potential by changes in the coupling constants and baryon form factors.

These potentials differ from one another in other interesting ways. Potential A28 has a $NN \leftrightarrow \Delta\Delta$ tensor potential from π exchange with an overall strength $f^2_{\pi\Delta N}/f^2_{\pi NN}$ relative to the NN tensor potential given the Chew-Low value of 4 [28]. The potential function has a Yukawa form corre-

TABLE I. Decay width $\Gamma(d^*)$ in MeV in the didelta model of the d^* for different baryon-baryon interactions.

Potential	$P_D(\%)$	π only	$\pi+\rho$	$f^2_{\pi\Delta N}$ [a]	Λ_π [b]	Λ_ρ [b]	Specials
A28	6.13	100		0.324			
BC	5.61	133	57	0.221	3.0	1.7	
		132	58				G
		56	21				G/ΔM
BB	4.99	101	38	0.224	1.7	1.85	
		98	38				G
		41	12				G/ΔM
CC3	4.87	30	20	0.35	0.8	1.35	ΔM
		21	13				G/ΔM
BA	4.38	79	17	0.229	1.3	1.95	
		74	15				G
		31	4				G/ΔM
FB	4.25	68	44	0.224	1.2	1.4	
		62	40				G
		26	15				G/ΔM
		76	17		1.3	1.4	(1,1)
		71	15				G
		29	4				G/ΔM

[a]Dimensionless.
[b]In GeV.

sponding to a meson propagator $1/\omega^2(q)$ in momentum space, where $\omega^2(q)=q^2+m^2_{\rm meson}$. Its short-distance cutoff is specified in coordinate space using a function that bends the potential back to the origin to simulate the contribution of ρ exchange [29].

The Bonn potentials use nucleon form factors for the cutoff, with a monopole form for the π vertex and usually a dipole form for the ρ vertex. The cutoff masses Λ_i used are shown in the table. The meson (m) coupling constants used here for the Bonn A, B, and C potentials [18], denoted here as potentials BA, BB, and BC, and for the ''full'' Bonn potential FB [27], are the quark-model values based on the ratio $f^2_{m\Delta N}/f^2_{mNN}=72/25$ [28]. Potentials BA, BB, and BC are relativistic momentum-space potentials. FB is a relativistic model with energy-dependent meson propagators. The coupled-channel III, denoted here as CC3, is nonrelativistic and uses a strong-coupling ratio of about 4.4.

The second numerical entry given in the first line for each potential is the width calculated with the π exchange only of the potential. The result is clearly correlated with cutoff mass Λ_π in the Bonn potentials. It decreases roughly monotonically from 130 MeV to only 30 MeV as we go from potential BC to BB, BA, Full Bonn (FB), and CC3 potentials as Λ_π decreases from 3.0 to 0.8 GeV.

When the ρ-exchange contribution is added, the resulting width, shown as the third numerical entry in the first line, decreases dramatically to the range of 57–20 MeV. The trend appears to be correlated with the decreasing value of the deuteron D-state probability P_D, except for the special case of potential FB discussed separately. It is of course the differences in P_D caused by different partial cancellations by the ρ-exchange potential that distinguish between these potentials in the first place.

The result for the FB potential is different because the $NN\leftrightarrow\Delta\Delta$ potential generated by a simple quark-model prescription is not that shown in the first line of the results given in the table for the FB potential, but on the fourth line, where the width of 17 MeV is in rough agreement with the value for potential BA and with the trend dictated by P_D. Note that the $\rho\Delta N$ form factor is a monopole, a difference noted in the table by the entry $[(n_\pi,n_\rho)=]$ (1,1) under the column ''Specials.'' The results of line 4 for the FB potential are also the results reported previously in [7].

In the actual FB potential, the meson-ΔN vertices are further modified: First, the $\rho\Delta N$ form factor is changed from a monopole to a dipole form with no change in the cutoff mass Λ_ρ. This change of the form factor causes the ρ contribtuion to be reduced significantly, thus causing an ''unexpected'' increase in the decay width.

A second change made in the actual FB potential is to decrease the cutoff mass Λ_π from 1.3 to 1.2 GeV. This change is dictated by the need to prevent the uncorrelated 2 π contributions to the potential in the lower partial waves from becoming unmanageably large [27], a situation that is not yet encountered in our lowest-order calculation. As far as our lowest-order result is concerned, Table I shows that the effect of this change is quite minor.

The widths for potential CC3 also stand out from the trend. Comparing them with those for potential BB, which has a comparable P_D, we can see that particularly the π contribution has been reduced significantly by the use of the much smaller cutoff mass, thus giving an abnormally small width in perturbation theory. Presumably, the channel-coupling potentials in CC3 will give rise to larger contributions from the long-range π-exchange potentials in higher orders. Hence it is likely that the large difference seen in the lowest-order calculation reported here will not persist so noticeably in higher orders.

To summarize, the d^* decay width appears to be controlled to a good extent by P_D, and has a value in the range 15–60 MeV. In comparison, the value of 100 MeV for potential A28 is more appropriate to π exchange only. In other words, the simulation of ρ exchange contained in it has not been very effectively in the long-distance part of the tensor potential that controls the decay width.

I now turn to the many remaining entries in Table I. The second line for each potential, or for each group within a potential, contains results obtained by replacing each cutoff factor $1/[1+(q^2/\Lambda^2)]$ by the Gaussain $\exp[-(q^2/\Lambda^2)]$. This change, marked in the column ''Specials'' by the symbol G, improves the high-momentum behavior of various momentum integrals and also reduces the overestimate of the high-momentum wave function in our perturbative treatment. Its influence on our decay widths is minimal, except in potential CC3 where the small cutoff mass Λ_π allows a relatively large effect.

In using the potential models discussed here, we either use the given coordinate-space potential $v(r)$ or the standard meson propagator $1/\omega^2(q)$, plus corrections from vertex form factors. The exception is the coupled-channel model

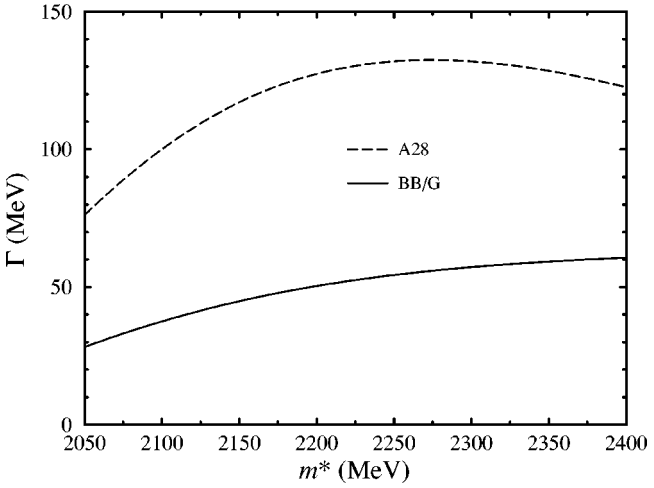

FIG. 5. The decay width Γ of d^* as a function of the d^* mass m^*.

CC3 of [18], for which we use the off-shell propagator

$$\mathcal{P}(q)=\omega^{-1}(q)[\omega(q)+\Delta M]^{-1}, \tag{29}$$

defined in the potential. Here $\Delta M=M_\Delta-M_N$.

The question could be raised as to whether one should use the off-shell propagator in these cross-channel potential as a general policy. Taken by itself, the answer is probably no. The reason is that the standard propagator leads to energy-independent Yukawa potentials that are actually superior to energy-dependent potentials arising from the use of off-shell propagators. It is not obvious, but the use of an energy-independent potential actually corresponds to the inclusion of that component of the two-baryon state having a virtual meson ''in the air'' [30,31].

Although the use of the off-shell propagators is not recommended, it is clear that their use will reduce the decay width calculated with the standard propagators. To study the size of the reduction, I now repeat the calculation with off-shell propagators. The results are shown on the third line of each group, and marked by the symbol ΔM under the ''Specials'' column. We see that this off-shell effect is quite large, especially on the π-exchange contributions. As a result, there is much closer cancellation than before between the π and ρ contributions, thus giving rise to a much smaller net decay width.

In subsequent calculations in this paper, I shall use the A28 potentials to give an extreme case, and the BB/G potential for a more representative example, of the results expected for the electroproduction T factors. The decay widths calculated for these two potentials are shown in Fig. 5 as functions of the dibaryon mass m^*. Gaussian vertex form factors are used in potential BB/G.

With these calculated widths, the $^3D_3$ component can now be estimated more reliably by perturbation theory. The results are given in Fig. 4 as long dashed (solid) curves for potential A28 (BB/G) using $m^*=2100$ MeV and the calculated value of $\Gamma=100$ MeV (38 MeV). Both the smooth part $h^*(p)$ and the complete radial wave function $\psi(NN\,^3D_3,p)$ of Eq. (27) are shown. The perturbative normalization in this state for potential BB/G is $P_3=4.5\%$.

The perturbative result for $\psi(\Delta\Delta\,^7D_1,p)$ of Eq. (25) calculated for potential BB/G is also given in Fig. 3 as a thick dashed curve when only the π-exchange part of the potential is included in the calculation, and as a thick solid curve when the ρ exchange contribution is also included. The large reduction in the wave function caused by the inclusion of ρ-exchange is worthy of note. The perturbative normalization in this state for the complete BB/G potential is $P_7=0.38\%$.

C. Electroproduction T factors

The inelastic production amplitudes from the dominant deuteron $NN(^3S_1)$ component to the $NN(^3D_3)$ component of d^*, as described by diagram 1(c), can finally be calculated. The major difference from the procedure described in Sec. III is that the radial wave function $\psi_3\equiv d^*(NN\,^3D_3)$ is now too complicated to be expanded readily in terms of harmonic-oscillator wave functions. It is kept in numerical form so that the final result, instead of being entirely analytic, now requires a one-dimensional numerical integration.

To simplify the calculation, the deuteron $d(^3S_1)$ wave function is expressed as a sum of three Gaussians. However, results need to be given only for a single Gaussian. For this purpose, I use the notation of Eq. (11), but with unstarred parameters. All production amplitudes then have the generic form

$$\langle d(^3S_1)\|\hat{\mathcal{O}}(q)\|d_3^*\rangle=c_0N_0e^{-(q/2)^2/2\beta^2}e^{-\alpha_0q^2/2}\times\int e^{-p^2/2\beta^2}\psi_3(p)f_{\mathcal{O}}(p,q)p^2dp, \tag{30}$$

but different integrand functions

$$\begin{aligned}f_{\mathcal{O}}(p,q)&=j_2\quad(\text{for }\hat{M}_2)\\&=\frac{\sqrt{6}}{M_N}\frac{2\beta^2}{q}j_2\quad(\text{for }\hat{T}^{\text{el}}_{c2})\\&=-\frac{\mu_s(N)}{M_N}\frac{c_1}{\sqrt{6}}\left[\left(\frac{q}{4}+\frac{4\beta^2}{q}\right)j_2-ipj_1\right]\quad(\text{for }\hat{T}^{\text{el}}_{\mu2})\\&=\frac{\mu_s(N)}{M_N}\frac{2}{\sqrt{21}}\left[\left(\frac{q}{4}+\frac{10\beta^2}{q}\right)j_2-ipj_1\right]\quad(\text{for }\hat{T}^{\text{mag}}_{\mu3}).\end{aligned} \tag{31}$$

Here $j_i\equiv j_i(ipq/\beta^2)$ is a spherical Bessel function, and $c_0=\sqrt{7}$, $c_1=1$.

The production amplitudes from diagram 1(a) have a similar form, but with $c_0=\sqrt{3}$, $c_1=4$, and of course different radial wave functions. The baryon magnetic-moment parameter that appears is now $\mu_s(\Delta)$ instead of $\mu_s(N)$. I have verified explicitly that they give the same numerical values as the oscillator expressions given in Sec. III. The difference

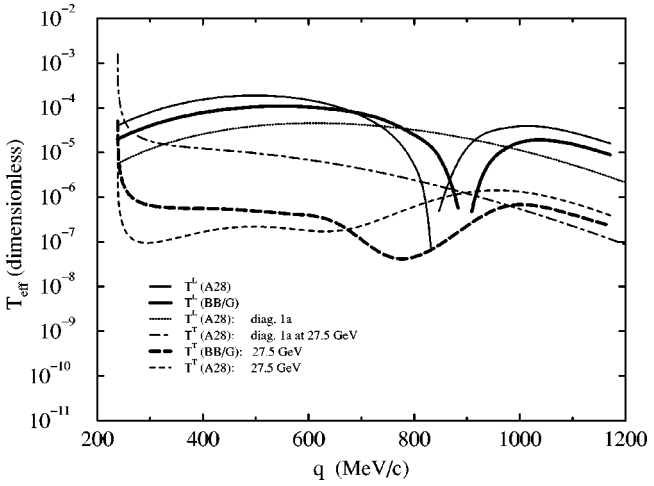

FIG. 6. Comparison of the effective T factors in the electroproduction cross section of d^* from the deuteron as calculated from diagrams 1(a) and 1(c) for potential A28 and from diagrams 1(b) and 1(c) for potential BB/G at the electron laboratory energy of 27.5 GeV with the results for diagram 1(a) alone for potential A28.

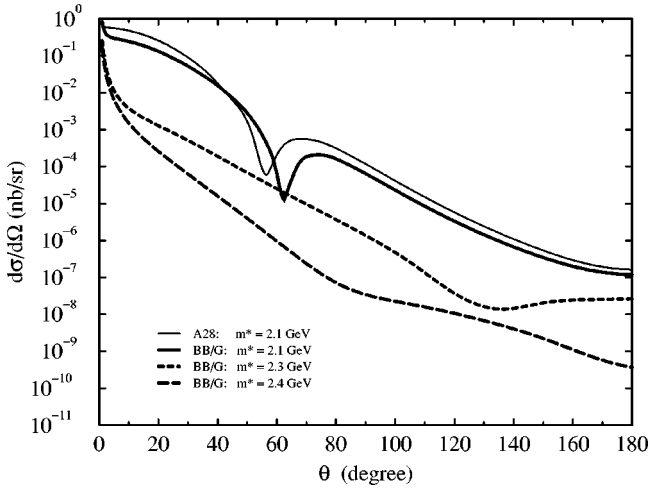

FIG. 7. Integrated differential cross sections $d\sigma/d\Omega$ in the laboratory for the production of d^* from deuteron for 1 GeV electrons calculated for potentials A28 and BB/G at different dibaryon masses m^*.

in the numerical coefficients c_α comes from the recoupling of angular momenta. These alone favor the amplitudes from diagram 1(c) by a factor of roughly $\sqrt{7/3}$, which is ratio of two 6j-symbols.

To perform the calculation for potential BB/G, I use a three-term approximation to the BB deuteron $NN(^3S_1)$ wave function [18]. The resulting perturbative deuteron $\Delta\Delta(^7D_1)$ wave function calculated from Eq. (25) is fitted to a 4-term harmonic-oscillator form. Both fitted wave functions are given in the Appendix. This fitted $\Delta\Delta(^7D_1)$ wave function is the one shown as a thick solid curve in Fig. 3.

The calculated effective T factors are shown in Fig. 6 with the curves defined in the legend.

We can see that electroproduction RMS's from diagram 1(a) (in the case of A28) or 1(b) (BB/G) and diagram 1(c) interfere destructively at small q values. At $q = 300$ MeV/c, for example, the production amplitude that contributes to the Coulomb factor T^L from diagram 1(c) for potential A28 is opposite in sign and about 3.6 times larger than that from diagram 1(a). Of the increase, a factor $\sqrt{7/3}$ comes from a 6j symbol, while the remaining factor of 2.4 comes from the wave functions in a radial integral. Hence T^L is about 7 times that for diagram 1(a) alone.

The production amplitude from diagram 1(c) varies more strongly with the momentum transfer because of the much stronger momentum dependence of the $d^*(NN\,^3D_3)$ wave function it contains. This production amplitude changes sign just below $q = 1000$ MeV/c where the curve for diagrams 1(a) and 1(c) crosses that for diagram 1(a) alone the second time. This is above the interference zero that can be seen in Fig. 6. After the sign change, the amplitudes from the two diagrams add constructively.

In the effective transverse T factors for potential A28, the production amplitudes from the two diagrams are of comparable magnitudes but opposite signs at low momentum transfers. The resulting destructive interference is very severe, causing the total contribution to $T_{\rm eff}$ to be some two orders of magnitude smaller than that from diagram 1(a) alone. The interference eventually becomes constructive at roughly the same momentum transfer as for the Coulomb T^L factor.

The results for the BB/G potential are qualitatively similar, but the Coulomb T^L factor is smaller at the smaller momentum transfers.

V. RESULTS AND DISCUSSION

For all electron energies greater than a few GeV, the effective T factors are essentially energy independent. The remaining factors in the integrated differential production cross section $d\sigma/d\Omega$ of Eq. (1) do depend on the energy, however. Since this energy dependence is well known, it is sufficient to show results for one energy only.

The calculated angular distributions are shown in Fig. 7 for 1 GeV electrons. The result for potential A28 is for diagrams 1(a) and 1(c), while those for potential BB/G are for diagrams 1(b) and 1(c). The interference between the two diagrams can be visualized more readily by also examining Fig. 8 which show additional results for potential BB/G from diagram 1(c) alone.

For the dibaryon mass $m^* = 2.1$ GeV, the sharp local minima near 60° comes from the amplitude zero in the Coulomb T^L factor. When diagram 1(c) appears alone, this zero comes from the sign change in the $d^*(NN\,^3D_3)$ wave function. When both diagrams 1(b) and 1(c) are included, it comes from an interference zero in the sum of their amplitudes. The two diagrams interfere destructively below the sharp minimum and constructively above it. For example, the integrated cross section at the laboratory angle of 30° is 0.05 nb/sr for potential BB/G, but 0.11 nb/sr for diagram 1(c) alone.

The overestimate of the cross section by potential A28 can be seen in Fig. 7. At the laboratory angle of 30°, the

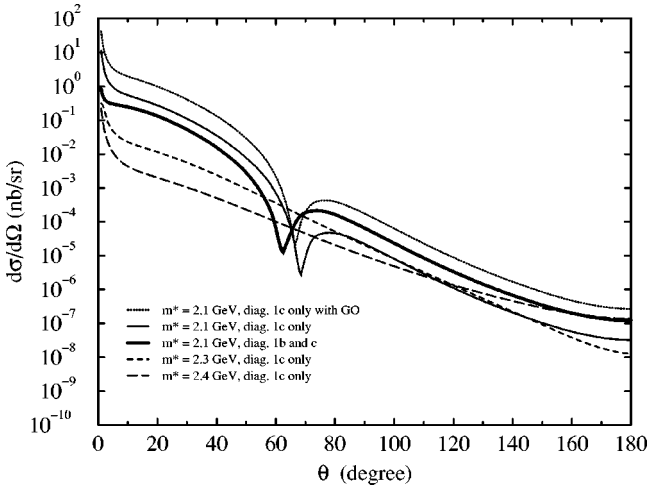

FIG. 8. Integrated differential cross sections $d\sigma/d\Omega$ in the laboratory for the production of d^* from deuteron for 1 GeV electrons calculated for potential BB/G at different dibaryon masses m^* when only diagram 1(c) is included. The dotted curve gives the result when the perturbative $d^*(NN\,^3D_3)$ wave function is calculated using the potential GO instead. For comparison, the result for $m^*=2.1$ GeV when both diagrams 1(b) and 1(c) are included is shown as a thick solid curve.

cross section of 0.09 nb/sr for potential A28 is about twice as large as the value for potential BB/G. Other than this, both cross sections show the same decreasing trend with increasing laboratory angle.

The Mott cross section σ_M and the target recoil factor $f_{\rm rec}$ do not depend on the dibaryon mass m^*. However, the magnitude of four-momentum transfer decreases as m^* increases, while that of the three-momentum transfer increases. This leads to a rapid decrease in the kinematical factor $v_{\rm L}$.

The dynamical factor $T_{\rm eff}$ also changes with m^*. This is partly because of the three-momentum transfer appearing in it and partly because the d^* wave function $d^*(NN\,^3D_3)$ itself also changes. The interference between the two diagrams becomes rather complex. The Coulomb T^L factor decreases rapidly with increasing m^*. At $m^*=2.3$ GeV, the minimum in the angular distribution at 135° is caused by the interference zero in both T^L and T^T. At $m^*=2.4$ GeV, the shallow minimum near 90°, comes from the combined effects of an interference zero in T^T at 100° and an interference zero in T^L at 50°. The destructive interference between the two production amplitudes at small momentum transfers tends to become more severe as m^* increases.

Figure 7 shows how rapidly the cross section decreases with increasing m^*. At the laboratory angle of 30°, the integrated cross section with both diagrams present, which at 0.05 nb/sr is already small for $m^*=2.1$ GeV, now falls down to only 0.0005 (0.00006) nb/sr for $m^*=2.3$ (2.4) GeV, as shown in Fig. 7.

The very small calculated cross sections obtained for both larger angles and larger m^* suggest that the present lowest-order picture might not be adequate under these circumstances. A much more elaborate calculation that includes higher-order diagrams as well as additional production processes important at these larger three-momentum transfers might have to be considered.

The result reported here can be compared with a recent calculation by QSW [19], who include diagram 1(c) and 1(a) production amplitude going to the $NN^*(1520)$ component of d^*. They find that diagram 1(c) dominates the calculated cross section for 1 GeV electrons scattered to a laboratory angle of 30°, and obtain a preliminary value for the integrated cross section greater than 10 nb/sr there.

In order to compare with QSW, we show in Fig. 8 our result for diagram 1(c) alone at the same $m^*=2.1$ GeV but calculated with potential BB/G. Our cross section is only 0.11 nb/sr at 30°, two orders of magnitude smaller.

One difference between the two calculations is that the baryon-baryon interaction used by QSW comes from [10] and contains only the π-exchange contribution. In potential A28 and certainly in the Bonn potentials used here, the baryon-baryon tensor potentials are significantly reduced by cancellation against additional ρ-exchange contributions.

To isolate the contribution of π exchange alone, we repeat the calculation for diagram 1(c) alone with only one modification — using the interaction of [10] (called here potential GO) to generate the perturbative $d^*(NN\,^3D_3)$ wave function. The potential GO has the coupling constant $f^2_{\pi\Delta N}=0.36$ $(=f^{*2}/4\pi$ in the notation of [10]), roughly consistent with those shown in Table I. A monopole form factor for the $\pi\Delta N$ vertex is used with the cutoff parameter $\Lambda_\pi=1250$ MeV. The $^3S_1$ wave function used in this calculation remains that of the Bonn B deuteron. This is not very different from the Bonn C wave function used by QSW.

The resulting cross section, for $m^*=2.1$ GeV, is shown in Fig. 8 as a dotted curve. The calculated cross section at 30° is 0.41 nb/sr, almost 4 times bigger than the BB/G result. This shows that the neglected ρ-exchange contributions do reduce the cross section significantly.

The situation remains qualitatively the same when diagram 1(a) is also included: The cross section for potential GO at 30° is 0.29 nb/sr, a factor of 6 greater than the value of 0.05 nb/sr for potential BB/G.

The cross sections for diagram 1(c) alone for potential BB/G calculated with $m^*=$ 2.3 and 2.4 GeV are also given in the figure and compared with the results for $m^*=$ 2.1 GeV with only diagram 1(c) and with both diagrams present.

After accounting for the difference in dynamical inputs, I find a remaining discrepancy of more than an order of magnitude between my calculation and that of QSW. This remaining difference must be due to differences in the calculational methods used. The most important difference seems to be my use of a principal-value Green's function in my $d^*(NN\,^3D_3)$ wave function compared to the use of an outgoing-wave boundary condition in QSW. The QSW calculation thus gives an additional term in the production amplitude from diagram 1(c) that contains an energy-conserving δ function. This additional term has a part that is the decay amplitude of $d^*(\Delta\Delta)$ into the NN channel. I do not include this part as the physical electroproduction production amplitude. Additional studies must be made to understand if this could account for all the remaining disagreement.

Returning to the general problem of calculating the elec-

troproduction cross section of d^*, there are of course the additional uncertainties in the predicted mass and structure of d^* itself. Given the experimental nonobservation of $I=0$ dibaryons in the mass range 2.00–2.23 GeV [16], future experimental searches and theoretical studies should probably move to higher masses. For electroproduction, the rapid decrease of the cross section with increasing d^* mass is a cause of concern if it persists in higher-order calculations.

The theoretical uncertainty in the d^* structure remains a major obstacle. The didelta model of d^* used here is very crude, and may not be adequate at short distances where the baryons overlap. Other exotic components in the deuteron wave function must also be taken into consideration, especially at the larger momentum transfers. The possibility of quark delocalization and color screening remains an open question, but the failure to see any d^* dibaryon in the experiment of [16] is discouraging.

All these issues make it clear that much more work remains to be done before a quantitative description of the d^* production cross section can be achieved, given any theoretical model for d^*. The preliminary study given in this paper does suggest that the electroproduction cross sections to d^* are likely to be very small.

Perhaps more interestingly, the existence of d^* at low masses can now be viewed from a rather elementary perspective. Consider a very naive model of d^* containing a probability $P_{\Delta\Delta}(d^*)$ of the $\Delta\Delta(^7S_3)$ configuration and the remaining probability, $1-P_{\Delta\Delta}(d^*)$, of a closed-channel configuration that does not decay at all into any channel. The two pieces of information—(a) that the best available experimental upper bound of 0.08 MeV obtained by [16] for its decay width into the NN channel near 2.1 GeV and (b) that the best theoretical estimate of its width of about 40 MeV given in this paper if d^* is a didelta—if taken literally, would require that $P_{\Delta\Delta}(d^*)$ cannot exceed something of the order of 0.2%. This seems to suggest that any model of d^* containing a much larger $P_{\Delta\Delta}(d^*)$ might already have been excluded by the measurements of [16].

ACKNOWLEDGMENTS

I wish to thank Fan Wang, Terry Goldman, Stan Yen, Earle Lomon, Bob Wiringa, Faqir Khanna, and R. Dymarz for many stimulating conversations and correspondence. I am indebted to Stan Yen for asking about the resonance contribution to the total cross section measurement of Lisowski *et al.* [16] that led to the experimental upper bound given in the Introduction.

TABLE II. Wave functions used in the calculation.

Wave function	Parameters
$d^*(NN\,^7S_3)$	$\boldsymbol{\beta}^2=$ 2.0753 (1, 1.25, 1.46) fm^{-2}
	$\mathbf{c}$ = (14.8312, -27.4124, 13.3505)
	100.19%→100.00%
$d(NN\,^3S_1)$ A28	$\boldsymbol{\beta}^2=$ 0.04056 (1, 7.25, 169)
	$\mathbf{c}$ = (0.5250, 0.5900, -0.0573)
	93.17%→93.31%
$d(NN\,^3S_1)$ BB	$\boldsymbol{\beta}^2=$ 0.02298 (1, 5.15, 21.9)
	$\mathbf{c}$ = (0.3192, 0.4859, 0.3486)
	95.04%→95.01%
$d^*(\Delta\Delta\,^7D_1)$ A28	$\boldsymbol{\beta}^2=$ 0.1769 (1, 5.0, 15.0)
	$\mathbf{c}$ = (0.00118, 0.01537, 0.05407)
	0.4182%→0.4190%
$d^*(\Delta\Delta\,^7D_1)$ BB/G	$\boldsymbol{\beta}^2=$ 0.9395 (1, 3.18, 8.26, 28.0)
	$\mathbf{c}$ = (0.00316, 0.02245, 0.02422, 0.02955)
	0.379%→0.383%

APPENDIX: WAVE FUNCTIONS USED IN THE CALCULATION

Many of the wave functions used have been fitted to the form

$$\psi(p)\approx\sum_{i=1}^{3} c_i\psi_i(p), \tag{A1}$$

where $\psi_i(p)$ is a normalized HOWF's like that shown in Eq. (13), with the falloff parameter

$$\boldsymbol{\beta}^2=(\beta_1^2,\beta_2^2,\ldots). \tag{A2}$$

The dimensionless expansion coefficients are

$$\mathbf{c}=(c_1,c_2,\ldots). \tag{A3}$$

In order to emphasize the stronger high-momentum components in these short-distance wave functions, the range parameters are obtained by minimizing the *percentage* mean-square deviation.

The fitted parameters are given in Table II. Each fitted wave function has been renormalized in order to change the raw percent probability to the value the original wave function has, as indicated in the third line of the table for each state.

[1] C.W. Wong and K.F. Liu, Phys. Rev. Lett. **41**, 82 (1978).
[2] R.L. Jaffe, Phys. Rev. Lett. **38**, 195 (1977).
[3] LISS (Light Ion Spin Synchrotron) White Paper, 1995, Indiana University Cyclotron Facility at http://www.iucf.indiana.edu/Publications/LISS.html
[4] T. Goldman, K. Maltman, G.T. Stephenson, Jr., K.E. Schmidt, and F. Wang, Phys. Rev. C **39**, 1889 (1989); F. Wang, J.L. Ping, G.H. Wu, L.J. Teng, and T. Goldman, *ibid.* **51**, 3411 (1995).
[5] F. Wang, G.H. Wu, L.J. Teng, and T. Goldman, Phys. Rev. Lett. **69**, 2901 (1992).
[6] T. Goldman, K. Maltman, G.T. Stephenson, Jr., J.L. Ping, and F. Wang, Mod. Phys. Lett. A **13**, 59 (1998).
[7] C.W. Wong, Phys. Rev. C **57**, 1962 (1998).

[8] D. Qing, Ph.D. thesis, Nanjing University, 1997.
[9] H.-M. Sun, Ph.D. thesis, Nanjing University, 1997.
[10] J.A. Gomez Tejedor and E. Oset, Nucl. Phys. **A571**, 667 (1994); **A580**, 577 (1994); **A600**, 413 (1996).
[11] J.A. Gomez Tejedor, E. Oset, and H. Toki, Phys. Lett. B **346**, 240 (1995).
[12] E.L. Lomon, nucl-th/9710006.
[13] E.L. Lomon (private communications).
[14] C.W. Wong, Phys. Rev. C **58**, 2414 (1998).
[15] C.W. Wong, Phys. Rev. C **60**, 038201 (1999).
[16] P.W. Lisowski, R.E. Shamu, G.F. Auchampaugh, N.S.P. King, M.S. Moore, G.L. Morgan, and T.S. Singleton, Phys. Rev. Lett. **49**, 255 (1982).
[17] R.B. Wiringa, R.A. Smith, and T.L. Ainsworth, Phys. Rev. C **29**, 1207 (1984).
[18] R. Machleidt, in *Advances in Nuclear Physics*, edited by J.W. Negele and E. Vogt (Plenum, New York, 1989), Vol. 19, p. 189.
[19] D. Qing, H.-M. Sun, and F. Wang, nucl-th/9912069.
[20] T. deForest, Jr. and J.D. Walecka, Adv. Phys. **15**, 1 (1966).
[21] T.W. Donnelly and A.S. Raskin, Ann. Phys. (N.Y.) **169**, 247 (1986).
[22] H. Uberall, *Electron Scattering from Complex Nuclei* (Academic Press, New York, 1971), Pt. A, pp. 248–249.
[23] R.B. Wiringa (private communications).
[24] R. Dymarz and F.C. Khanna, Nucl. Phys. **A516**, 549 (1990).
[25] A.N. Ivanov, H. Oberhummer, N.I. Troitskaya, and M. Faber, nucl-th/9912032.
[26] D. Allasia *et al.*, Phys. Lett. B **174**, 450 (1986).
[27] R. Machleidt, K. Holinde, and Ch. Elster, Phys. Rep. **149**, 1 (1987).
[28] G.E. Brown and W. Weise, Phys. Rep., Phys. Lett. **22C**, 279 (1975).
[29] A.M. Green and P. Haapakoski, Nucl. Phys. **A221**, 549 (1974).
[30] B. Desplanques, Phys. Lett. B **203**, 200 (1988).
[31] C.W. Wong, Phys. Rep. **242**, 149 (1994).